# Frequency-modulated impulse response photothermal detection through optical reflectance. 2: Experimental

Joan F. Power and Andreas Mandelis

A fast thermoreflectance impulse response photothermal imager was assembled and tested with several solid materials [quartz, stainless steel, and polyvinylidene difluoride (PVDF)]. The instrument was found to yield quantitative data in agreement with Green's function theoretical models of time domain heat conduction. The FM chirp laser intensity modulation technique used in these experiments gave wide bandwidth photothermal signals and was found to be only limited by the FFT instrumentation frequency response (100 kHz). Thermal diffusivities were calculated, while thermal lensing and thermoelastic effects were further observed. The imager was thus shown to be capable of replacing pulsed laser devices for truly nondestructive applications with materials with low damage threshold to optical pulses.

## I. Introduction

The modern development of photoacoustic and photothermal sciences has spawned a generation of thermal wave technologies whose impact on the field of nondestructive evaluation is currently being felt. Recently, thermal wave techniques have formed the basis for a growing field of photothermal microscopy in which micron-sized structures may be examined in solid samples.[1-3] The use of lasers to induce thermal wave propagation in materials and the heavily damped short-range character of thermal waves are responsible for the micron-sized resolution capabilities of photothermal microscopy. Furthermore, photothermal microscopy offers the unique capability for obtaining depth resolved images of consecutive material layers in a sample, owing to the varying depths of penetration of sinusoidally modulated thermal energy as a function of frequency.

The conventional methods for the detection of thermal waves in solids have used gas microphone photoacoustic cells and piezoelectric transducers.[4] The gas microphone cell, while a high sensitivity device, is limited in bandwidth to below 10 kHz and suffers from response nonlinearities primarily due to acoustic resonances. This bandwidth limitation severely restricts the depth resolution of the technique. Piezoelectric devices, on the other hand, exhibit good high frequency response but require mechanical coupling to the sample and exhibit nonflat transfer functions at resonant frequencies. Consequently, neither of these detection methods is fully capable of the wideband noncontact detection of thermal waves. The alternative technique of thermal wave detection through optical reflectance measurements has proved to be such a wideband noncontact method,[5] when used with pump laser beam modulation in the frequency domain. Several disadvantages of the conventional method of single frequency concerning the imaging resolution of that technique as well as substrate damage threshold considerations with the use of pulsed lasers have been discussed elsewhere.[6,7]

A third strategy exists for obtaining a transient thermal response, which avoids the possibility of optical damage to the sample and facilitates the theoretical interpretation of signals. Wideband strategies, which involve sample excitation by a wavetrain possessing a flat power spectrum, yield high resolution impulse and frequency response information via correlation and spectral analysis. The excitation energy is delivered to the sample over a large duty cycle so that a large overall energy may be delivered at very low power. Wideband FM strategies have been recently demonstrated in both photothermal[8-10] and photopyroelectric spectrometry[11-13] and yield high quality band-limited impulse response information at low power.

In the present work, we applied the high performance wideband excitation technique of frequency modulation time delay spectrometry described in Part 1 to optical reflectance thermal wave measurements and obtained thermal impulse response information

When this work was done both authors were with University of Toronto, Department of Mechanical Engineering, Photoacoustic & Photothermal Sciences Laboratory, Toronto, Ontario M5S 1A5, Canada; Joan Power is now with McGill University, Chemistry Department.

Received 1 December 1987.
0003-6935/88/163408-10$02.00/0.

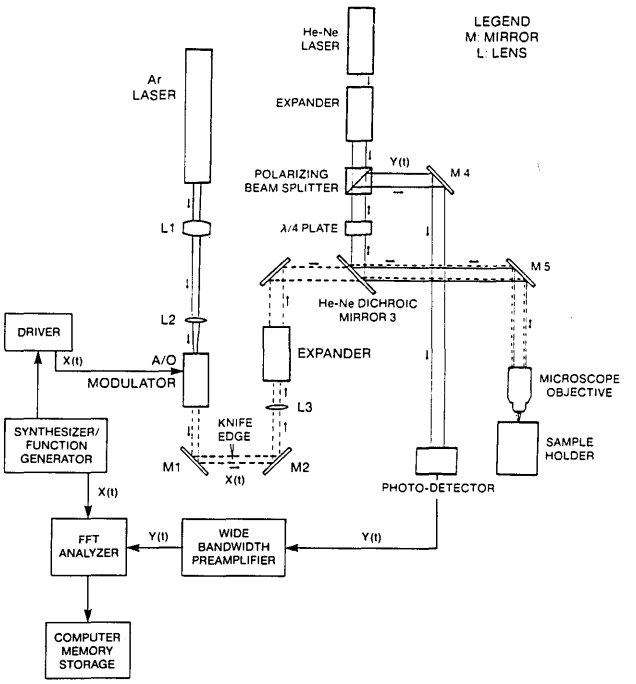


Fig. 1. Block diagram of wide-bandwidth impulse response photothermal wave instrumentation. $X(t)$ and $Y(t)$ are real-time system input and output waveforms, respectively.

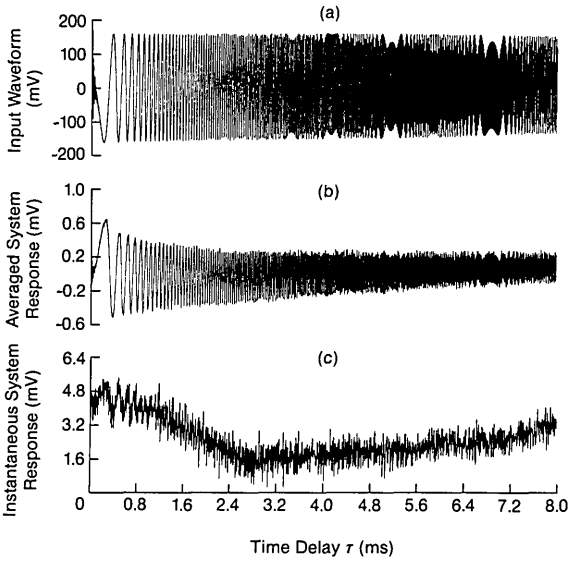


Fig. 2. Linear FM sweep wavetrains for photothermal (reflectance) response of a semi-infinite quartz sample. Sweep/measurement bandwidth: $\Delta f$ = 0–100 kHz. Sweep rate, $S = 1.25 \times 10^7$ Hz/s; window: uniform (a) excitation sweep $x(t)$; (b) response waveform $y(t)$. Averaging $N$ = 1000 records for (a),(b); (c) instantaneous $y(t)$ record with no averaging.

on some well-characterized samples. We also demonstrate the implementation of the wideband technique in thermal diffusivity measurements and the conditions in which quantitative information may be obtained.

## II. Experimental

### A. Apparatus

Figure 1 shows a block diagram of the apparatus used for the detection of thermal waves by optical reflectance modulation. The basic optical design was previously reported by Opsal *et al.*[1] in earlier modulated cw thermal wave experiments, whereas the associated instrumentation forms the basis for our real-time impulse response photothermal imager. Excitation was obtained from a Coherent Innova 90 argon-ion laser, which was operated single line at 488 nm. The $Ar^+$ beam was fed through an acoustooptic (AO) modulator where its intensity was time varied by drive signals supplied by the internal function generator of an HP3562A FFT analyzer. The drive waveforms were linear FM sweeps (see Refs. 11–13 for details on signal recovery). Figure 2 shows typical excitation and response waveforms. The first-order output of the modulator was isolated using a knife-edge directed through a beam expander and combined with the probe beam by means of a dichroic beam splitter. Probe light was obtained from a 4-mW He–Ne laser (Melles-Griot) at a wavelength of 632.8 nm. The probe beam was directed through a beam expander and a polarizing beam splitter. The polarizing splitter transmitted linearly polarized light. The transmitted vertically polarized component was then directed through a quarterwave plate to obtain a circularly polarized beam. The circularly polarized probe beam was combined collinearly with the $Ar^+$ beam on the dichroic mirror, directed through a microscope objective with a magnification of 50, and focused onto the sample surface. The reflected component of the probe beam had a circular polarization of the opposite orientation to that of the incident beam: interference of the reflected and incident components at the quarterwave plate produced a horizontally polarized beam returning into the detection path, consisting of a mirror, optical narrowband filter, and the quad cell detector (UDT model SPOT-4D). The quad cell signals reported in this work were recorded in the sum mode. The quad cell output was applied to the $y(t)$ input of the FFT analyzer, while the $x(t)$ input was obtained directly from the output of the internal sweep generator. A gating pulse synchronous with the initiation of each frequency sweep was used to trigger the acquisition of time records at the $x(t)$ and $y(t)$ inputs to the HP 3562A. Time averaging of 300–1000 records was carried out to improve SNRs. Impulse response information was recovered from the frequency sweep data by means of correlation and spectral functions computed by the HP 3562A waveform analyzer. The signal bandwidth of the instrument was 100 kHz.

The samples examined in this work consisted of specimens of quartz, stainless steel, and polyvinylidene difluoride (PVDF). The quartz specimens were surface deposited with a thin (5000-Å) layer of gold to promote surface absorption and reflection. Stainless steel samples were prepared by milling. The PVDF film (28-$\mu$m thickness) was used as supplied from Pennwalt Corp.[14]

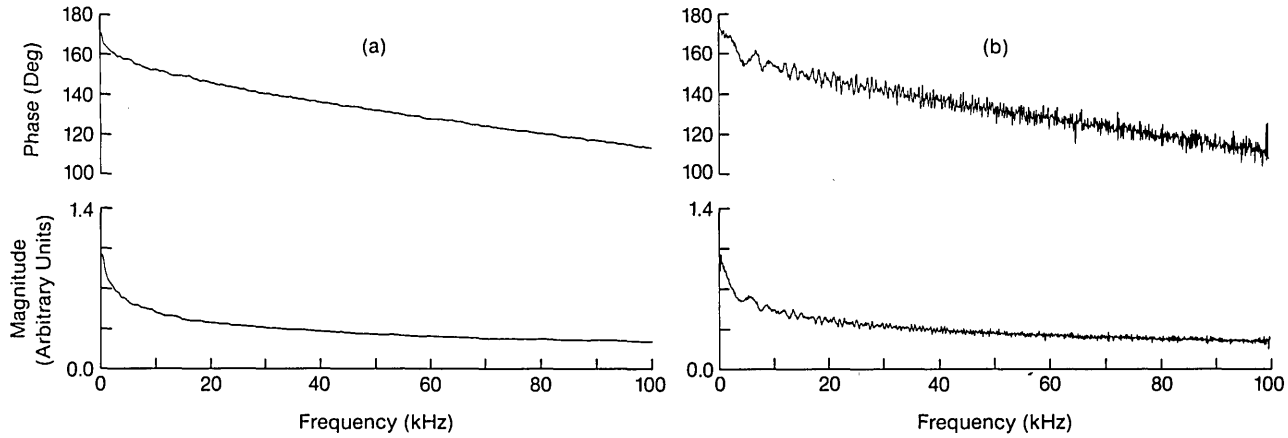


Fig. 3. Frequency response profiles via (a) point-by-point slow sine sweeps of the sample's transfer function $H(f)$. Magnitude and phase. (b) FM linear sweep response $H(f)$, magnitude and phase. Frequency span 0–100 kHz. In (a) the sweep rate was 1.1 kHz/s with 50-ms integration period per point. Resolution: 499 Hz. Number of averages = 25. In (b) the sweep rate was $1.25 \times 10^7$ Hz/s; window: uniform. Sample was semi-infinite quartz.

### B. Results

The photoinduced thermoreflectance measurements reported in the present work have as their basis the monitoring of changes in a sample's reflectance $R$ due to changes in temperature following light absorption. The reflectivity change has the form[6]

$$\Delta R = R - R_0 = \left(\frac{\partial R}{\partial T}\right)_{T=T_0} \Delta T, \tag{1}$$

where $\Delta R$ is the reflectivity change at the sample surface, $R_0$ is the unperturbed surface reflectivity, and $\partial R/\partial T$ is the sample's temperature coefficient of reflectance. The temperature change $\Delta T$ is given by

$$\Delta T = T(r,z = 0,t) - T_0, \tag{2}$$

where $T_0$ is the ambient temperature and $T(r,z,t)$ is the temperature distribution in the sample. The analytical form of $T(r,z,t)$ has been derived from theory in Part 1, for several cases relevant to the present work.

A direct proportionality between $\Delta R$ and $T(r,z,t)$ is predicted by Eq. (1), so that the reflectivity changes recorded in a typical experiment are a direct monitor of the surface temperature.

The detection of thermal waves by optical reflectance modulation is in principle a simple process, which suffers in practice from a number of interfering photothermal phenomena. These competitive effects include thermoelastic deformations of the sample and thermal blooming phenomena,[15] which take place at the sample surface following light absorption. Careful optimization of the irradiation and detection geometry is required to minimize these effects. In addition, the effect of varying the relative sizes of the pump and probe beams, as well as the introduction of an offset between the beam centers, has significant repercussions on the recovered photothermal signals. Before comparing theory and experiment, a number of these phenomena are examined, and their origins are discussed.

## III. Signal Analysis and Measurement Performance

It is first necessary, before analyzing in detail the variations in the recovered broadband photothermal response signals, to establish the absence of artifacts in the measurement system and signal analysis procedures. In the first case, the linear sweep excitation used to recover impulse and frequency response information has been known, in some cases,[16] to depend on the sweep rate $S$. This could potentially arise because of the slow speed of response of diffusive linear systems, typical of the present photothermal case. By comparing point-by-point frequency response measurements made using very low sweep rates, with results recovered from high speed linear FM chirps, it was possible to eliminate the sweep rate as a significant variable in the ranges of signals studied (Fig. 3). Measurements recovered over the maximum frequency span of the analyzer (0–100 kHz) at a rate of $1.25 \times 10^7$ Hz/s agreed to within experimental error with frequency response measurements made point by point in the frequency domain, using both slow sine sweeps and lock-in detection, as shown for a semi-infinite sample of quartz, whose response profile is representative of the samples studied. The rippling artifact observed in the FM chirped frequency response profile of Fig. 3(b) is due to second- and higher-order harmonic components in the acoustooptic modulator output but has been shown to make only a minor contribution to the observed frequency response. Overall these results point to the absence of direct computational biases in the signal analysis procedure.

A second factor to be examined was the flatness of the frequency response of the quad cell detector and its internal preamplifiers. The detection system frequency response reported in Fig. 4 was recorded by modulating a laser beam directly on the quad cell aperture. The recovered response shows good magnitude flatness with a small phase offset, which is linear in frequency. Because other errors (discussed below) dominate to a greater extent, these effects were noted,

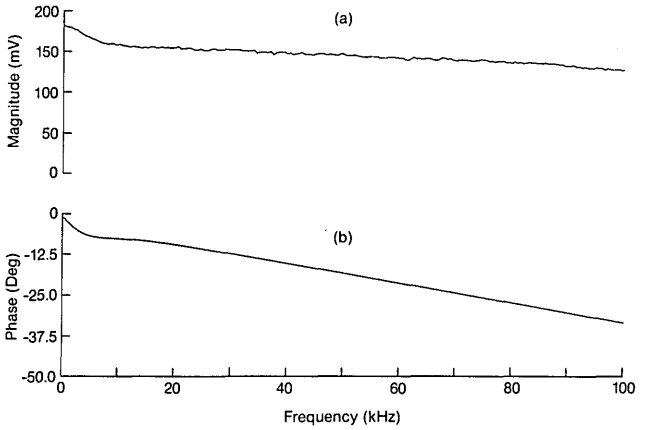


Fig. 4. Transfer function $H(f)$ recorded for a quad cell detector system. Measurements were made with a slow sine sweep from 100 Hz to 100 kHz. The frequency scale was swept point by point with 50-ms integration time per point. Resolution was 499 Hz. Sweep rate: 1.1 kHz/s. (a) Magnitude; (b) phase.

but no correction of the recovered photothermal data was made for detector response.

The frequency response profiles reported in Fig. 3 for the semi-infinite quartz sample contain a significant magnitude component at 100 kHz, which corresponds to the upper limit of the analyzer bandwidth. Clearly the photothermal signal components extend beyond the span limit of the analyzer. This is expected due to the wide response bandwidth of thermoreflectance and thermoelastic effects. The latter are shown later in this work to contribute significantly to the measured photothermal signals. The thermoreflectance effect, itself a pure thermal response, also contains significant signal components at frequencies above 100 kHz for most of the samples studied in this work. The finite contribution of signals to the magnitude $|H(f)|$ of the transfer function at the span edge (100 kHz) has been implicated as a prime source of the Gibbs phenomenon observed in the recovered impulse response profiles (Fig. 5). This arises because the

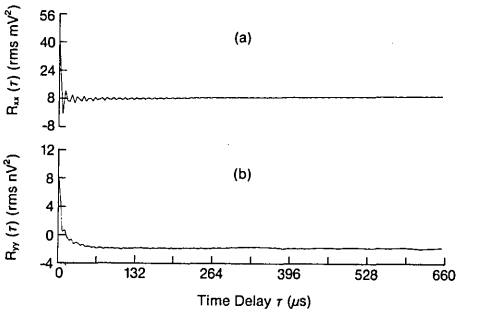


Fig. 6. Evaluation of measurement performance: (1) $R_{xx}(\tau)$, (b) $R_{yy}(\tau)$ for semi-infinite quartz sample: $\Delta f = 0$–100 kHz; $S = 1.25 \times 10^7$ Hz/s.

impulse response $h(\tau)$ is recovered by direct inverse Fourier transformation of $H(f)$, which contains an effective truncation at 100 kHz. In some cases, multiplication of the frequency response by a logarithmic window eliminates much of this truncation error while apparently preserving thermal signal information [Figs. 5(a) and (c)]. The problems associated with the analyzer bandwidth limitation are further demonstrated in Fig. 6, which compares the input and output cross-correlation functions for the same quartz sample. Clearly the approximation of $R_{xx}(\tau)$ to a Dirac $\delta$ function is poor since the input pulse width is not of very short duration relative to the pulse width of $R_{yy}(\tau)$. Again, this phenomenon arises because of the presence of high frequency signal components at and above 100 kHz. Depending on the detailed beam geometries for irradiation and on the thermal properties of the sample studied, these high frequency components will contribute to a greater or lesser extent. The above considerations apply directly to any semi-infinite sample with a thermal response approaching the form $T \propto 1/t^{3/2}$, which corresponds to a pure 3-D heat conduction process[6] and approaches the upper limit of detection bandwidth required for measurements on a semi-infinite sample.

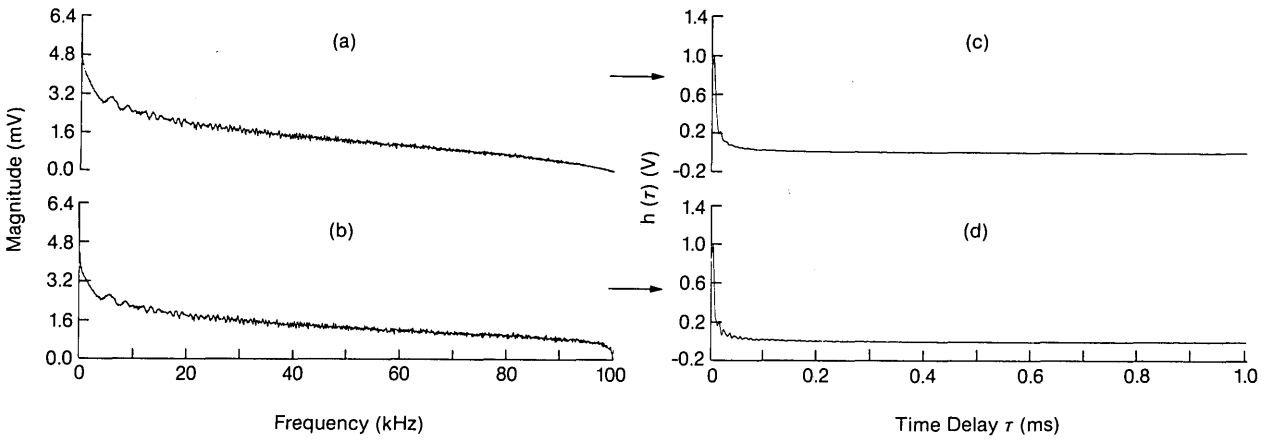


Fig. 5. Time-domain Gibbs phenomenon observed by truncation of frequency response data: windowing effects on the transfer function $H(f)$ and on the impulse response $h(\tau)$. (a) $|H(f)|$ windowed by a function with a gradual cutoff. (b) The same $|H(f)|$ windowed by a function with a sharp rolloff (phase response not shown). (c), (d) Impulse responses corresponding to (a), (b), respectively. Sample was semi-infinite quartz. Data were recovered from a linear FM sweep with $\Delta f = 0$–100 kHz, $S = 1.25 \times 10^7$ Hz/s, and $N = 1000$ averages.

## IV. Irradiation Geometry

The next set of factors to be examined is concerned with the irradiation geometry for the thermoreflectance measurement. The theory developed in Part 1 assumed that the thermal profile in the sample was set up via irradiation by a pump beam with spot size $w_0$. No account was taken of the size or location of the probe beam. In practice, the thermoreflectance measurement is made with a probe beam of spot size $w_1$ and Gaussian transverse intensity profile $\exp(-r^2/w_1^2)$ intercepting the heated region of the sample surface. Furthermore, the probe beam may be offset from the pump beam in alignment by a few microns, defined by a radial offset $r_b$. The quad cell detector, operating in the sum mode, integrates the probe intensity over an aperture with dimensions large relative to $w_1$. This situation is described theoretically by integrating over the transverse coordinates:

$$h(t) = \int_0^{\infty} \int_0^{2\pi} T(\bar{r},z = 0,t) \exp(-r^2/w_1^2) r dr d\theta, \tag{3}$$

where $h(t)$ is the sum signal observed from the quad cell, $T(r,0,t)$ is the thermal profile at $z = 0$, and $\bar{r} = r - r_b$, where $r_b$ is the center of the probe beam.

The simplest case to be studied experimentally is the case of a semi-infinite sample. The temperature profile $T(r,0,t)$ has in that case the form[6]

$$T(\bar{r},z = 0,t) = \frac{A_0}{(4\alpha t + w_0^2)t^{1/2}} \exp\left[-\frac{(r - r_b)^2}{4\alpha t + w_0^2}\right], \tag{4}$$

where

$$A_0 = \frac{P_0 w_0^2 \alpha^{3/2}}{2\pi^{3/2}},$$

$P_0$ is the irradiance of the incident laser beam, $w_0$ is the radius of the pump beam, and $\alpha$ is the thermal diffusivity of the sample. Integrating over the radial coordinate gives a quad cell signal of the form

$$h(t) = \frac{A_0 \tau_0}{2(t + \tau_1)t^{1/2}} \exp\left[-\frac{r_b^2}{4\alpha(t + \tau_1)}\right], \tag{5}$$

where

$$\tau_1 \equiv \frac{1}{4\alpha}(w_1^2 + w_0^2); \qquad \tau_0 \equiv \frac{w_1^2}{4\alpha}.$$

The constants $\tau_0$ and $\tau_1$ have the dimensions of time and correspond to diffusional thermal transit times to the offset distances $w_1$ and $(w_1^2 + w_0^2)^{1/2}$, respectively, from the center of the optical excitation (pump beam). If the beam alignment is concentric, $r_b = 0$, and Eq. (5) becomes

$$h(\tau) = \frac{A_0 w_1^2}{8\alpha(\tau + \tau_1)\tau^{1/2}}, \tag{6}$$

where the time-delay domain variable $\tau$ has been substituted for $t$.

The experimental effect of varying the relative sizes of $w_0$ and $w_1$ is illustrated in Fig. 7 and may be understood qualitatively from the forms of Eqs. (4) and (6). The effect of the pump beam size $w_0$ on the recovered response was discussed in detail in the first part of this work.[6] Increasing the pump beam size produces a gradual transition from a pure 3- to 1-D response

$$\left(T \propto \frac{1}{t^{1/2}}\right)$$

due to the reduction in the radial degrees of freedom of the conduction process. If the probe beam radius is kept small as $w_0$ is increased, this transition from 3- to 1-D thermal decay is observed.

If, on the other hand, the pump beam radius is kept small, while the probe beam radius is increased, the effective aperture for integration of the signal increases since the factor $\exp(-r^2/w_1^2)$, in Eq. (3), broadens with increasing $w_1$. Physically, we have a situation in which the probe beam profile samples an increasingly larger radial area. The increasing radial component of heat flow in the sample is weighted by the probe beam and integrated by the quad cell as described in Eq. (3). This increased radial thermal contribution has the effect of broadening the impulse response profile, because the time required for thermal energy to propagate to a specified radial offset is given by

$$\tau_d = \frac{w_1^2}{6\alpha},$$

as can be shown[6] from Eqs. (3) and (6). Therefore, increasing the radial area integrated over produces a broadening or a delay contribution in the impulse response profile due to an increased weighting of these delayed radial components in the total response. As the probe beam size $w_1$ approaches infinity, the time-delay profile $h(\tau)$ approaches the form $1/t^{1/2}$, i.e., the form of a 1-D thermal decay in a semi-infinite medium.

These trends may be noted from Fig. 7, which reports the experimental impulse response signals observed as $w_0$ and $w_1$ are varied for a semi-infinite sample of quartz. As either $w_0$ or $w_1$ is increased, the

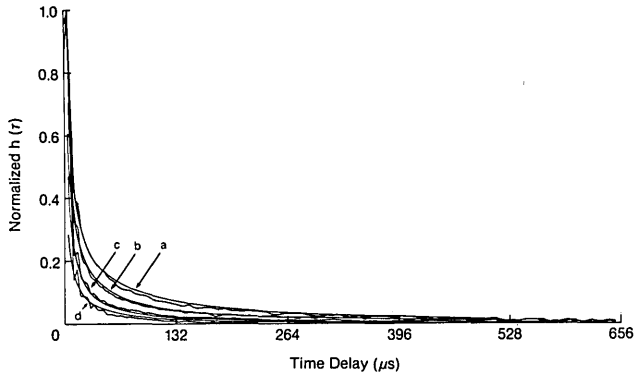


Fig. 7. Normalized impulse response profiles [$h(\tau = 0) = 1$] for a semi-infinite quartz sample with various values of $w_0$ and $w_1$. Theory vs experiment. Upper curve: (a) $w_0 = 14\,\mu m$, $w_1 = 12\,\mu m$; (b) $w_0 = 10\,\mu m$, $w_1 = 8\,\mu m$; (c) $w_0 = 8\,\mu m$, $w_1 = 2\,\mu m$; (d) $w_0 = 2\,\mu m$, $w_1 = 6\,\mu m$ (bottom curve). These results were obtained with linear FM chirp excitation and $\Delta f = 0$–$100$ kHz; $S = 1.25 \times 10^7$ Hz/s. Theoretical curves, Eq. (6), were fitted assuming that $\alpha = 5 \times 10^{-7}$ m$^2$/s for quartz. Experimental curves are the result of 1000 averages. Beam diameters were estimated independently.

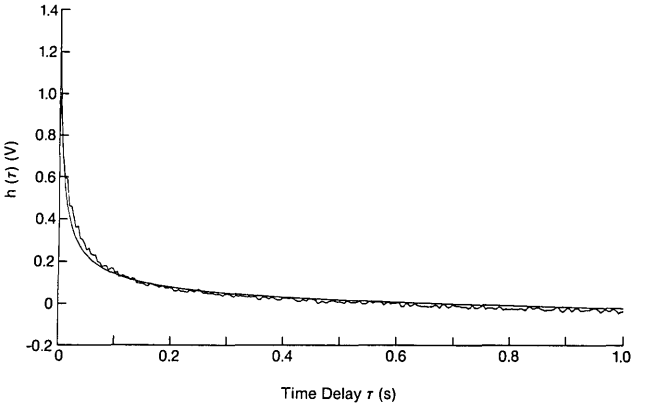


Fig. 8. Thermal blooming observed at the surface of a semi-infinite sample. Impulse response profile for thermal lens with expected 3-D theoretical response superimposed. Measurements were made with sweep rate, $S$ = 12.5 Hz/s and $\Delta f$ = 0–100 Hz.

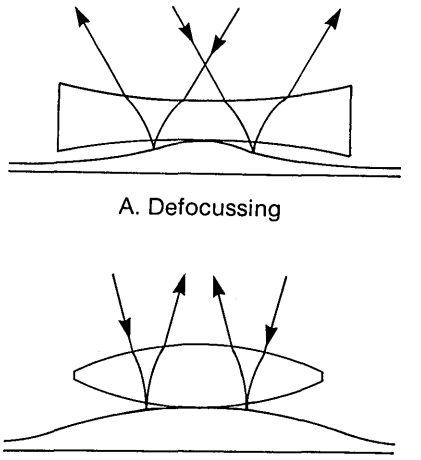


Fig. 9. Ray traces showing schematic of probe beam refraction and thermal lens formation above the sample surface in the gas phase: (A) Defocusing: forms of dark annulus in the probe beam center; (B) collimation: forms a bright spot at the center of the probe beam.

impulse response profile broadens showing a greater contribution of the longer time delay processes associated with radial conduction. Experimentally, very fast time decay signals are observed for the condition $w_0 \approx w_1 \approx 5\ \mu$m. This case minimizes the radial flow effects just discussed as well as the tendency for the thermal response to approach the 1-D condition as either $w_1$ or $w_0$ is increased. More details on the fitting of these results to the theory are discussed below.

An additional complication of the thermoreflectance signal is observed when the pump and probe beams are radially offset from each other. For metallic and most crystalline materials, this error in beam positioning is undetectable within the bandwidth of the present instrumentation, since the radial time-delay components $r_b^2/4\alpha$ are very small for beam offset errors of several microns. This is not always the case for highly insulating samples such as polymer films with $\alpha \leq 1 \times 10^{-7}$ m$^2$/s. An offset error as low as 2 $\mu$m can result in a significant radial delay component.[6]

## V. Competitive Photothermal Effects

### A. Thermal Lensing

Two important phenomena complicate the thermoreflectance measurement process. These effects consist of (a) thermal lens formation due to the diffusion of heat into the gas layer above the sample surface and (b) thermoelastic deformations of the sample. Both effects have been investigated in detail in the frequency domain by Opsal *et al.*[1] The thermal lens effect is easily detected in these experiments by visually monitoring the intensity profile of the probe beam as the pump beam irradiates the sample. Blocking and unblocking the pump beam cause the time-dependent formation and decay of an annular interference pattern near the center of the probe beam. The time scale for growth and decay of this refraction pattern is several hundred milliseconds, with the time dependence of this phenomenon being independent of the nature of the sample irradiated. This suggests that the common heat conduction process is gas phase related. An impulse profile for the thermal lens effect is shown in Fig. 8 together with the expected theoretical response. This signal has an approximate time dependence of the form $h(\tau) \propto 1/t^{3/2}$.

The observed annular interference pattern in the probe beam may be explained by the two refraction processes illustrated in Fig. 9. A thin layer of air at the surface is heated and expanded, causing a variation of the refractive-index profile of the gas layer. This profile behaves approximately like a lens, causing a refraction of the central section of the probe beam with the formation of the annulus.

The effect of thermal lensing on the recovered quad cell (sum) signal was examined by scanning an iris (~1-mm diameter) across a radial section of the annulus. As expected, an inversion of the $h(\tau)$ profile magnitude was observed as the interference pattern was scanned from the center section of the pattern to the rim of the annulus (Fig. 10). At the beam center, the time-dependent recovery of probe light is observed due to refraction by the lens consistent with the restoration of reflected power within the He–Ne laser probe aperture, following the collapse of the thermal lens at long times of the order of 1 s. Similarly, at the rim of the annulus, a time-dependent decrease in the probe beam intensity is seen at long times, as refracted power returns to the beam center following the collapse of the thermal lens. An intermediate behavior is observed at intermediate positions of the probe beam.

Both the temporal and power dependence of the thermal lens signal are distinct from the thermoreflectance and thermoelastic signals. It is well known[17] that the thermal lens effect saturates at relatively low powers due to departures from the formation of an ideal thin lens. The power dependence of the thermal lens effect was measured by recording the peak intensity of the $h(\tau)$ profile (at $\tau = 0$) as a function of the

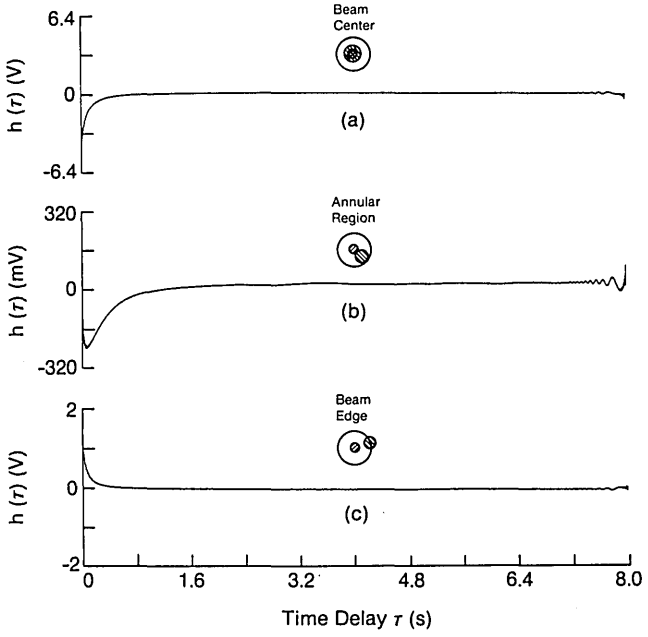


Fig. 10. Effect of spatial filtering of probe beam on the form of recovered thermal lens response: (a) response recovered with the center of annulus sampled; (b) response recovered with the rim of the annulus sampled; (c) response recovered with beam edge sampled. All measurements were made with a frequency sweep from 0 to 100 Hz at 12.5 Hz/s. Sample throughout was an oxidized Si wafer.

irradiation power. A comparison was made with the power dependence of the much faster thermoreflectance signal (Fig. 11). The thermal lens effect did saturate at relatively low power ($P \sim 60$ mW) as seen from Fig. 11(a), in general agreement with previous findings.[17] By contrast, the thermoreflectance effect is linear with irradiation power through 120 mW [Fig. 11(c)]. Opsal *et al.*[1] have reported in detail on the effect of thermal lensing on beam deflection measurements of thermoelastic signals. Their work clearly demonstrated that thermal effects contribute to the attenuation of thermoelastically induced probe beam deflections at frequencies up to 1 MHz. The mechanism of signal suppression appears to be the bending of the deflected beam by the refractive-index gradient or lens element above the sample surface. The refractive bending of the deflected beam induced by the gradient tends to offset the deflection produced by the thermoelastic effect.

Unless compensated by correct alignment procedures, thermal lensing potentially contributes to the thermal impulse response profile as well as the thermoreflectance effect,[1] albeit the time evolution of these physical processes varies widely. The annular interference pattern, induced in the probe beam as the result of thermal lens formation, clearly affects the spatial distribution of energy in the beam without in principle altering the integrated intensity. It is, therefore, essential that the entire transverse profile of the reflected probe beam be integrated by the detector. Blockage of only part of the beam center or a section of the annulus of the bloomed probe will yield a time-delay profile which contains a contribution due to the thermal lens-induced refraction, since this effect produces a time-dependent change in the spatial distribution of the probe beam energy.

### B. Modulated Thermoelastic Deformations

The absorption of a highly focused modulated laser beam at the surface of a solid sample produces two complementary effects: a thermoreflectance effect, detected by measuring the integrated intensity of the probe beam, and a thermoelastic effect, detected by monitoring beam deflection at the sample surface.

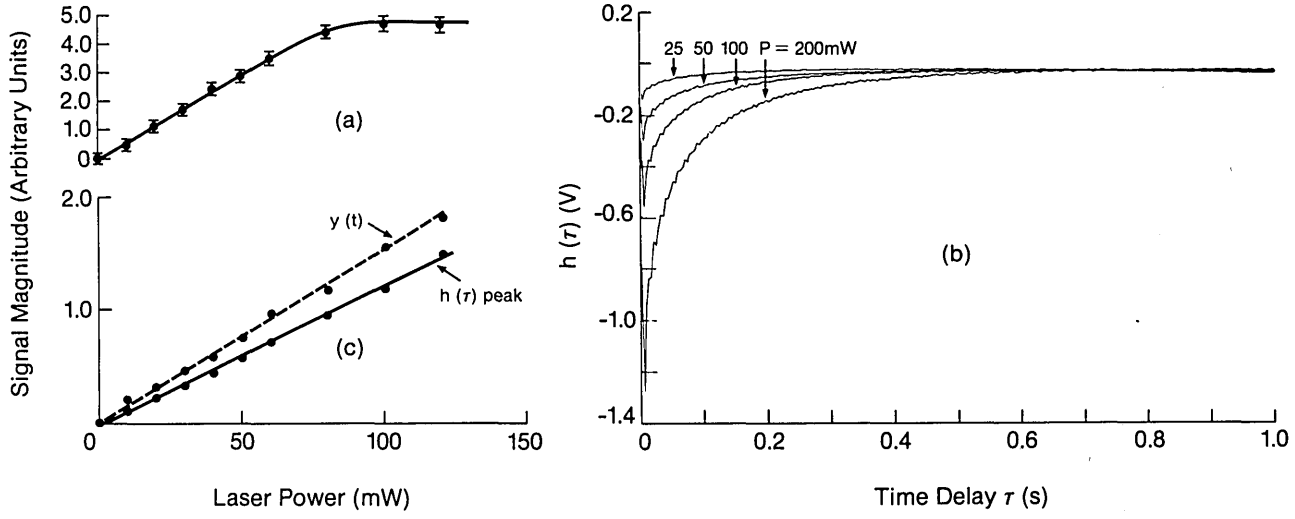


Fig. 11. Power dependence of (a), (b) thermal lens and (c) thermoreflectance signals. (a) Power dependence for the thermal lens effect was plotted as the peak value of the impulse response $h(\tau = 0)$ vs the modulated laser power level. Sample was semi-infinite quartz. (b) Impulse responses recovered at various incident beam powers for a semi-infinite sample of stainless steel. (a), (b) Measurements were made with linear FM sweeps from 0 to 100 Hz at 1.25 Hz/s and $N = 10$ sweeps. (c) Power dependence of reflectivity signal for semi-infinite quartz measured at the peak of impulse response $h(\tau = 0)$. These measurements were made with a linear FM sweep from 0 to 100 kHz at $1.25 \times 10^7$ Hz/s and $N = 1000$.

The deflection effect may be recorded as a change in the position of the reflected probe beam on the face of a quad cell detector. The quad cell records this positional change as a difference in intensity between its quadrants. Consequently, one measures, in principle, thermoreflectance signals via a quad cell operating in the sum mode and thermoelastic deformations via the quad cell's difference mode.

The detection strategy used in the present experiments was initially expected to separate thermoelastic from thermoreflectance signals, since sum mode signals are insensitive to beam position changes. However, a detailed analysis of the frequency and impulse response profiles recorded for the samples studied indicated a deviation from the thermoreflectance theory which was immediately assignable to a flatband contribution of an extraneous signal in the frequency domain. As shown in Fig. 12, a baseline of constant magnitude appears in the frequency response for a typical semi-infinite quartz sample. Tests of background noise levels in the experiment eliminated this factor as an explanation of the observed effect. The instrumental performance tests reported earlier also eliminate signal artifacts or aliasing as sources of this frequency baseline. On the other hand, this flatband response agrees well with the frequency response expected for the thermoelastic effect below 100 kHz.[2] Thermoelastic effects have been studied in the frequency domain for a variety of solid materials, by Opsal *et al.*,[1] and by Mandelis *et al.*[2] These previous works indicated that the thermoelastic frequency response is approximately flat below 100 kHz, which matches the detection bandwidth, and would explain the frequency baseline observed in the present work. Figure 12 shows experimental and fitted theoretical transfer functions for the semi-infinite quartz sample in two different focusing conditions. The theoretical curves consist of a thermal curve plus a flat baseline, which is consistent with the thermoelastic effect. The thermal result was obtained by fast Fourier transforming the corresponding theoretical time domain profile using parameters identical to those used in the experiment (sampling interval $\Delta f$, resolution, pump and probe beam sizes, and sample thermal diffusivity). The thermoelastic baseline was then estimated from the experimental curve using the relation (see Fig. 12)

$$\frac{|H_{\mathrm{th}}(100\ \mathrm{kHz})|}{|H_{\mathrm{th}}(500\ \mathrm{Hz})|} = \frac{|H_{\mathrm{exp}}(100\ \mathrm{kHz})| - x}{|H_{\mathrm{exp}}(500\ \mathrm{Hz})| - x}, \tag{7}$$

where $H_{\mathrm{th}}(f)$ stands for the theoretically calculated purely thermal transfer function, $H_{\mathrm{exp}}(f)$ represents the value of the experimental transfer function, and $x$ is the constant magnitude of the thermoelastic baseline. On normalization of the experimental and theoretical curves of Fig. 12 to the lowest frequency value at 500 Hz, Eq. (7) can be used to give an estimate for $x$:

$$|H_{\mathrm{th}}(100\ \mathrm{kHz})|_{\mathrm{Norm}} = \frac{|H_{\mathrm{exp}}(100\ \mathrm{kHz})| - x}{1 - x}. \tag{8}$$

As seen in Fig. 12, the resulting theoretical fits agree very well with the experimental curves, further strengthening the compatibility of the observed signals with a composite thermal/thermoelastic response model.

If thermoelastic effects do in fact explain the above results, a mechanism of signal detection is not immediately obvious. The use of the quad cell's sum mode signal for measurement would rule out beam deflection as a possibility in this case. If the flatband superposition is in fact produced thermoelastically, the induced motion or deformation of the sample surface must in some way vary the total measured intensity of the recovered probe beam at the detector. Further experimental evidence indicating that this effect is thermoelastically related is shown in Fig. 13, which compares frequency response measurements made on the

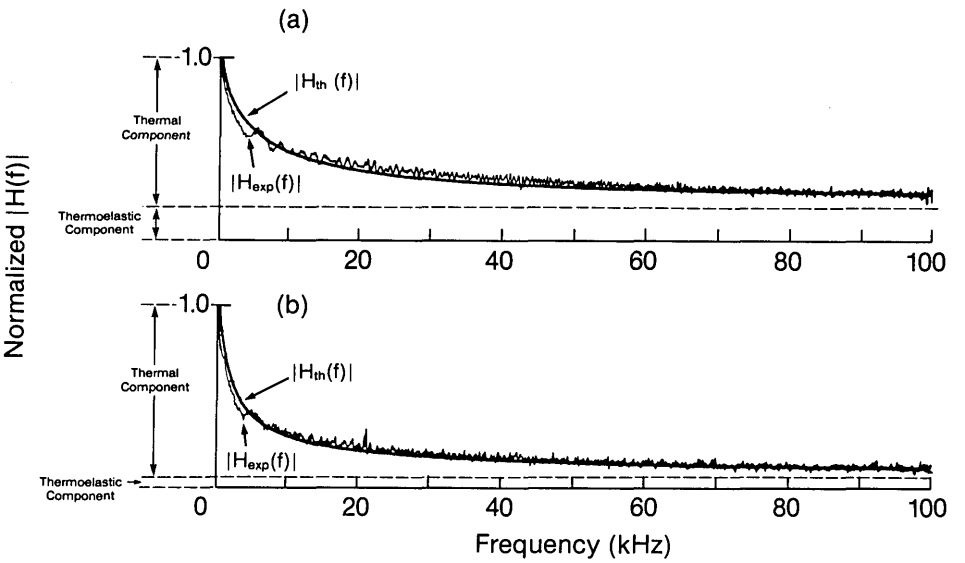


Fig. 12. Experimental transfer function $|H_{\mathrm{exp}}(f)|$ for semi-infinite quartz and theoretical fit $|H_{\mathrm{th}}(f)|$. The latter involves a superposition of a purely thermal response component and a constant thermoelastic baseline $x$: (a) $w_0 = 2\ \mu$m, $w_1 = 7\ \mu$m; $N = 500$ averages; (b) $w_0 = 14\ \mu$m, $w_1 = 12\ \mu$m; $N = 1000$ averages. $\alpha = 5 \times 10^{-7}$ m$^2$/s.

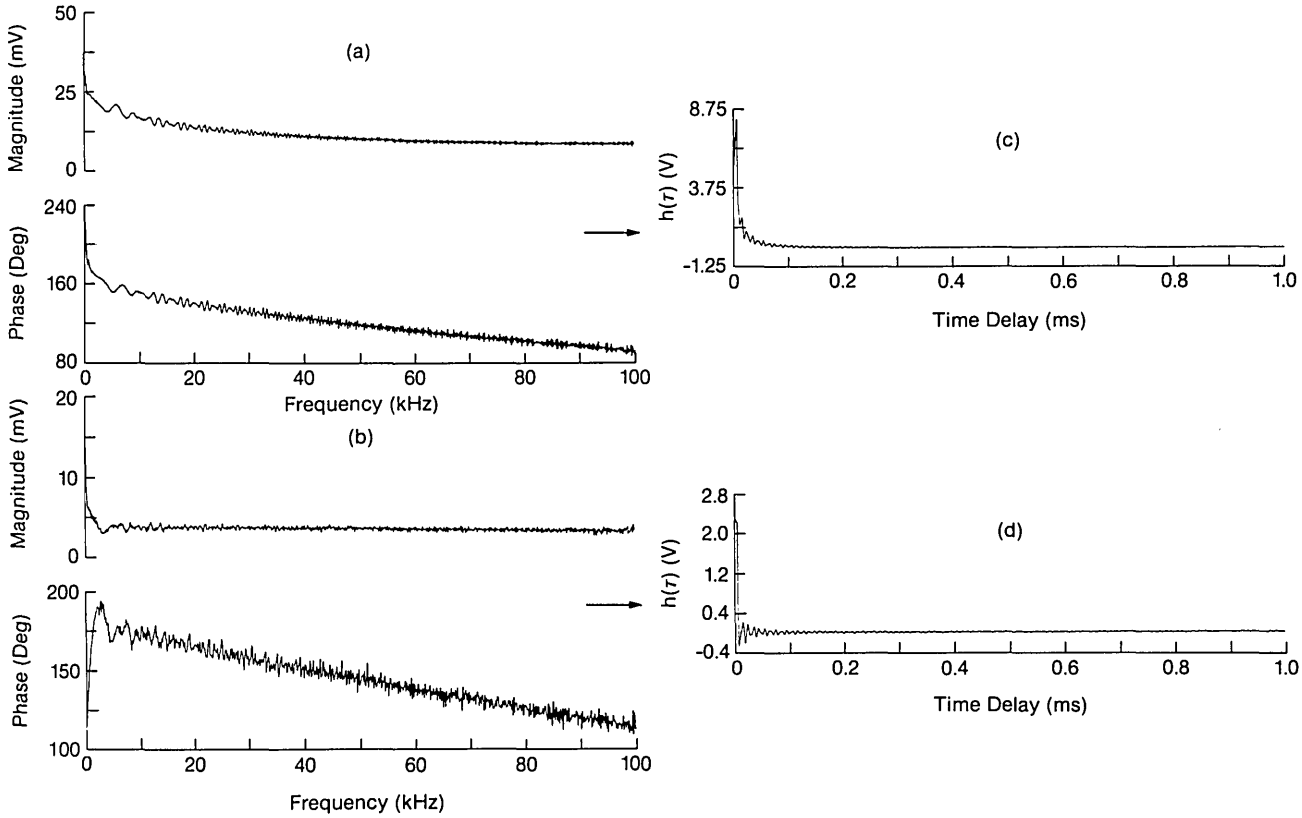


Fig. 13. Experimental frequency and corresponding impulse response measurements made with (a) pump and probe beams concentrically aligned; (b) probe beam offset from pump beam with $r_b > w_1$. The sample was semi-infinite quartz excited with a linear frequency sweep from 0 to 100 kHz at $1.25 \times 10^7$ Hz/s and $N = 300$ averages; (c), (d) impulse responses corresponding to (a), (b) measurements.

semi-infinite quartz sample in two separate conditions of beam alignment. Figure 13(a) gives the observed sum mode signal recovered when both pump and probe beams are concentrically overlapped. Figure 13(b) is the frequency response recovered when the two beams are completely separated. The separation of the two beams and the flatness of the response observed in Fig. 13(b) clearly point to a thermoelastic signal generating mechanism. The radial thermal profile drops off rapidly as a function of distance from the pump beam center so that direct thermoreflectance effects make a weak contribution in conditions of complete separation of the two beams. On the other hand, the frequency response observed in Fig. 13(a), corresponding to a concentric alignment of pump and probe beams, clearly shows a much larger weighting of signal components at the low frequencies, as is typical of the thermoreflectance response.

## VI. Thermal Diffusivity Measurements

The contributions of the beam radii in Eq. (6) allow for measurement of the thermal diffusivity on semi-infinite samples. For a given sample, variation of the beam profile characteristics gives rise to a family of impulse response curves as shown in Fig. 7. For the sake of convenience of reference, a halfwidth for the $h(\tau)$ profile may be defined as a means of estimating the width of the response curve. This halfwidth is defined here as the time delay at which the thermal impulse response $h(\tau)$ has decreased to half the initial value observed in the time record, which was set at 3.9 $\mu$s. The variation in the halfwidth of $h(\tau)$ with $w_0$ and $w_1$ is controlled by the thermal diffusivity $\alpha$, since this quantity determines the distribution of radial thermal transit times, which comprise the integrated quad cell response. For the semi-infinite quartz sample, which has a moderately low thermal diffusivity (Fig. 7), the variation in the halfwidth of the impulse response profile with beam radius is relatively large. For stainless steel, with 1 order of magnitude larger $\alpha$, this variation of $h(\tau)$ with $w_0$ or $w_1$ is suppressed, since radial thermal transit times across the beam coordinate are greatly reduced. Nevertheless, in both cases there is good agreement between literature values of the thermal diffusivity and those obtained from the thermoreflectance measurement (see Fig. 7 for quartz; similar theoretical fits to experimental impulse responses of a semi-infinite stainless steel sample yielded the value $4 \times 10^{-6}$ m$^2$/s for the thermal diffusivity of this material, in excellent agreement with the literature value[18] of $3.7 \times 10^{-6}$ m$^2$/s). An extended detection bandwidth would be required, however, to resolve differences in impulse response profiles for highly conducting materials such as aluminum ($\alpha \geq 1 \times 10^{-4}$ m$^2$/s). In this latter case, the thermal transit times are so small that very high frequency measurements (corre-

sponding to very early time delays) would be required to resolve differences in

$$\frac{w_1^2}{4\alpha} \quad \text{or} \quad \frac{w_0^2}{4\alpha}$$

in this regime.

In fitting the $h(\tau)$ data to Eq. (6), it was necessary to avoid the contribution due to the thermoelastic effect. For the quartz sample, the thermoelastic contribution appears as a delta function in the time-delay domain (Fig. 13). By fitting the data past the initial time-delay period of $\tau = 10$ $\mu$s it was possible to evaluate quantitatively the sample's thermal diffusivity independently of the thermoelastic contribution. This procedure is feasible for samples of moderately low thermal diffusivity. Highly conducting samples cannot be examined so successfully because much more of the thermal information appears at these early time delays.

Highly insulating materials such as plastics and macromolecular polymer samples have a large variation in $h(\tau)$ with $w_0$ and $w_1$ and appear to be promising candidates for this type of measurement. Unfortunately, they usually have a larger coefficient of thermal expansion and a dominating thermoelastic response. Long time scale heating of thin films may cause deformations of the irradiated surface with an accompanying vertical translation of the surface due to the thermoelastic effect. In this work, thermoreflectance measurements made on thin films of PVDF, ($\alpha = 6 \times 10^{-8}$ m$^2$/s), showed accompanying cyclic changes in the thermal impulse response as the film heated and deformed over a time scale of minutes. These slow deformations were sufficient to move the sample surface in and out of the focal plane of the microscope objective lens. Due to the very large variation in response of $h(\tau)$ with changes $w_0$ and $w_1$, surface motions of only a few microns over time could have been sufficient to produce these effects.

## VII. Conclusions

Most interesting applications of the thermoreflectance technique are in the thermal imaging of very shallow structures found in microelectronic devices. The bandwidth limitations of the present instrument (<100 kHz) do not permit the measurement or analysis of thermal profiles for structures in this size range. The present work does, however, establish the success of the wideband excitation technique as a means of providing thermal impulse response information and as a successful noncontact thermal diffusivity measurement technique. With an increased detection bandwidth, it should be possible to extend the analysis to very early time delays provided corrections are made for superposed thermoelastic effects.

The authors wish to acknowledge the financial support of the Natural Sciences and Engineering Research Council of Canada (NSERC) for several grants which made both parts (1 and 2) of this research possible.

## References

1. J. Opsal, A. Rosencwaig, and D. L. Willenborg, "Thermal-Wave Detection and Thin-Film Thickness Measurements with Laser Beam Deflection," Appl. Opt. **22,** 3169 (1983).
2. A. Mandelis, A. Williams, and E. K. M. Siu, "Photothermal Wave Imaging of Metal-Oxide-Semiconductor Field Effect Transistor Structures," J. Appl. Phys. **63,** 92 (1988).
3. A. Rosencwaig, "Thermal Wave Characterization and Inspection of Semiconductor Materials and Devices," in *Photoacoustic and Thermal Wave Phenomena in Semiconductors,* A. Mandelis, Ed. (North-Holland, New York, 1987), Chap. 5.
4. A. Rosencwaig, *Photoacoustics and Photoacoustic Spectroscopy* (Wiley, New York, 1980).
5. A. Rosencwaig, J. Opsal, W. L. Smith, and D. L. Willenborg, "Detection of Thermal Waves Through Optical Reflectance," Appl. Phys. Lett. **46,** 1013 (1985).
6. A. Mandelis and J. F. Power, "Frequency-Modulated Impulse Response Photothermal Detection Through Optical Reflectance. 1: Theory," Appl. Opt. **27,** 3397 (1988).
7. A. Mandelis, "Time-Delay-Domain and Pseudorandom Noise Photoacoustic and Photothermal Wave Processes: A Review of the State of the Art," IEEE Trans. **UFFC-33,** 590 (1986).
8. A. Mandelis, "Frequency Modulated (FM) Time Delay Photoacoustic and Photothermal Wave Spectroscopies. Technique, Instrumentation and Detection. Part I: Theoretical," Rev. Sci. Instrum. **57,** 617 (1986).
9. A. Mandelis, L. M. L. Borm, and J. Tiessinga, "Frequency Modulated (FM) Time Delay Photoacoustic and Photothermal Wave Spectroscopies. Technique, Instrumentation and Detection. Part II: Mirage Effect Spectrometer Design and Performance," Rev. Sci. Instrum. **57,** 622 (1986).
10. A. Mandelis, L. M. L. Borm, and J. Tiessinga, "Frequency Modulated (FM) Time Delay Photoacoustic and Photothermal Wave Spectroscopies. Technique, Instrumentation and Detection. Part III: Mirage Effect Spectrometer Dynamic Range and Comparison to Pseudo-Random-Binary-Sequence (PRBS) Method," Rev. Sci. Instrum. **57,** 630 (1986).
11. J. Power and A. Mandelis, "Photopyroelectric Thin Film Instrumentation and Impulse Response Detection. Part I: A Theoretical Model," Rev. Sci. Instrum. **58,** 2018 (1987).
12. J. Power and A. Mandelis, "Photopyroelectric Thin Film Instrumentation and Impulse Response Detection. Part II: Methodology," Rev. Sci. Instrum. **58,** 2024 (1987).
13. J. F. Power and A. Mandelis, "Photopyroelectric Thin Film Instrumentation and Impulse Response Detection. Part III: Performance and Signal Recovery Techniques," Rev. Sci. Instrum. **58,** 2033 (1987).
14. *KYNAR Piezo Film Technical Manual* (Pennwalt Corp., King of Prussia, PA, 1983).
15. J. P. Gordon, R. C. C. Leite, R. S. Moore, S. P. S. Porto, and J. R. Whinnery, "Long-Transient Effects in Lasers with Inserted Liquid Samples," J. Appl. Phys. **36,** 3 (1965).
16. H. Biering and O. Z. Pedersen, "System Analysis and Time Delay Spectrometry: Part II," Bruel Kjaer Tech. Rev. **2,** 1 (1983).
17. C. Hu and J. R. Whinnery, "A New Thermo-Optical Measurement Method and a Comparison with Other Methods," Appl. Opt. **12,** 72 (1973).
18. Y. S. Touloukian, R. W. Powell, C. Y. Ho, and M. C. Nicolaou, *Thermal Diffusivity* (IFI/Plenum, New York, 1973).